High Performance Organic Pseudocapacitors via Molecular Contortion

Jake C. Russell[1], Victoria A. Posey[1], Jesse Gray[1], Richard May[2], Douglas A. Reed[1], Hao Zhang[3], Lauren E. Marbella[2], Michael L. Steigerwald[1], Yuan Yang[4], Xavier Roy[1,*], Colin Nuckolls[1,*], Samuel R. Peurifoy[1,*]

[1] Department of Chemistry, Columbia University, New York, New York, USA.

[2] Department of Chemical Engineering, Columbia University, New York, New York, USA.

[3] Department of Chemistry, Beijing Key Laboratory of Advanced Chemical Energy Storage Technologies and Materials, Beijing, China.

[4] Department of Applied Physics and Applied Mathematics, Columbia University, New York, New York, USA.

* Corresponding authors: xr2114@columbia.edu, cn37@columbia.edu, s.peurifoy@columbia.edu

Pseudocapacitors harness unique charge storage mechanisms to enable high-capacity, rapidly cycling devices. Here we describe an organic system composed of perylene diimide and hexaazatrinaphthylene exhibiting a specific capacitance of 689 F/g at a rate of 0.5 A/g, stability over 50,000 cycles, and unprecedented performance at rates as high as 75 A/g. We incorporate the material into two-electrode devices for a practical demonstration of their potential as next-generation energy storage systems. We identify the source of this exceptionally high-rate charge storage as surface-mediated pseudocapacitance, through a combination of spectroscopic, computational, and electrochemical measurements. By underscoring the importance of molecular contortion and complementary electronic attributes in the selection of molecular components, these results provide a general strategy for the creation of organic high-performance energy storage materials.

The development of energy storage materials has traditionally focused on costly metal-containing solids.[1] Recent successes in fully organic energy storage materials[2] have galvanized interest in lightweight, affordable, and high-performance solutions to meet globally increasing energy demands.[3] Pseudocapacitors bridge the gap between secondary batteries and supercapacitors, leveraging a combination of electrical double-layer capacitance and surface-level Faradaic redox processes to store and release charge at rapid rates.[4] As a result, pseudocapacitors can provide higher power than batteries and higher energy

density than supercapacitors. However, most high-performance pseudocapacitors are fabricated from metal oxides, often requiring transition metals that are not Earth-abundant.[4] Fully organic pseudocapacitors are an inexpensive and green alternative, but until now, they have underperformed their inorganic counterparts.[5] These limitations are especially salient for electron-accepting materials used in negative electrodes, which are required for pairing with electron-donating materials in positive electrodes to achieve maximum performance in asymmetric cells.[6,7]

Here we report extraordinarily high pseudocapacitive performance from **PHATN** (perylene diimide – hexaazatrinaphthylene), an organic network fabricated from perylene diimide (PDI) and hexaazatrinaphthylene (HATN) whose synthesis and characterization are demonstrated in this work for the first time. These complementary molecular units were selected for their unique structures and robust electrochemical properties. PDIs are common and inexpensive industrial pigments.[8] Their use in electrochemical systems has been investigated extensively due to their notable stability, ease of derivatization, and ability to reversibly accept electrons.[9] HATN is a planar aromatic molecule exhibiting a high density of electroactive moieties[10] and synthetic flexibility.[11] In the design of **PHATN**, we demonstrate two major principles that may be generalized to other organic materials: 1) the selection of complementary electroactive components, in which each expands the voltage range and thus the charge storage capacity of the system, and 2) the contortion of the aromatic surface participating in pseudocapacitive behavior, which opens space for electrolyte and ion movement, leading to enhanced rate capability.

Figure 1a summarizes the material synthesis (see Methods for details). The polymerization of PDI and HATN building blocks into the scaffold **PHATN** utilizes a facile two-step strategy (Fig. 1a, b) based on Suzuki cross-coupling (Fig. 1c) followed by visible-light flow photocyclization (Fig. 1d).[12] The PDI building block is initially decorated with alkyl chains to facilitate solution processing. Once formed into the polymeric framework, these chains are removed via vacuum thermolysis, as shown by thermogravimetric analysis (TGA) and gas chromatography-mass spectrometry (GC-MS) of the condensate (Supplementary Fig. 5, 6). Solid state ^{13}C NMR (ssNMR) and IR spectroscopy confirm near-quantitative removal of alkyl chains (Extended Data Fig. 1a, Supplementary Fig. 7a) and retention of the imide moiety (Supplementary Fig. 7b). The resulting material (Fig. 1e) achieves best-in-class capacitance values of 689 F/g at a current density of 0.5 A/g, and performs well even at extremely high current densities (75 A/g), yielding capacitance values of over 430 F/g. These values are the highest of any reported negative electrode (i.e., electron-accepting) organic pseudocapacitor material and outperform even well-established positive organic pseudocapacitor architectures (Fig. 1f). To demonstrate a practical implementation of this material, we fabricated two-electrode hybrid energy storage cells from **PHATN** using activated carbon as the cathode; these cells display impressive specific energy and power. Overall, we find that the mechanistic origin of **PHATN**'s performance is the prevalence of surface-level redox events directly attributable to the molecular design principles outlined above.

The key structural feature underpinning **PHATN**'s performance is the contortion of the aromatic system, which simultaneously improves its ion mobility, exposed surface for ion association, and processability. These features are in sharp contrast with traditional planar systems in which strong π-stacking disrupts solubility and hinders ion mobility. The concept of molecular contortion is well-established within the field of organic electronics.[13,14] These established principles[15] are used to support our conclusions of contortion within **PHATN**, and explain the resulting emergent properties. The contortion of the aromatic system was spectroscopically and theoretically studied using a soluble model compound composed of one HATN unit and three PDI units (**PHATN monomer**, structure shown in Supplementary Scheme 4), as well as with an uncontorted control material, discussed later in the manuscript. NMR spectroscopy of **PHATN monomer** (Supplementary Fig. 3, 4) confirms the position of the cyclization, and DFT calculations reveal the contorted helical character of the structure (Extended Data Fig. 10, Supplementary Figs. 29-30). Although **PHATN** is composed of two planar aromatic systems, steric interaction at the imide position and a proximal hydrogen on the HATN linker (labeled H_a in Fig. 1d) forces the aromatic network out of planarity.

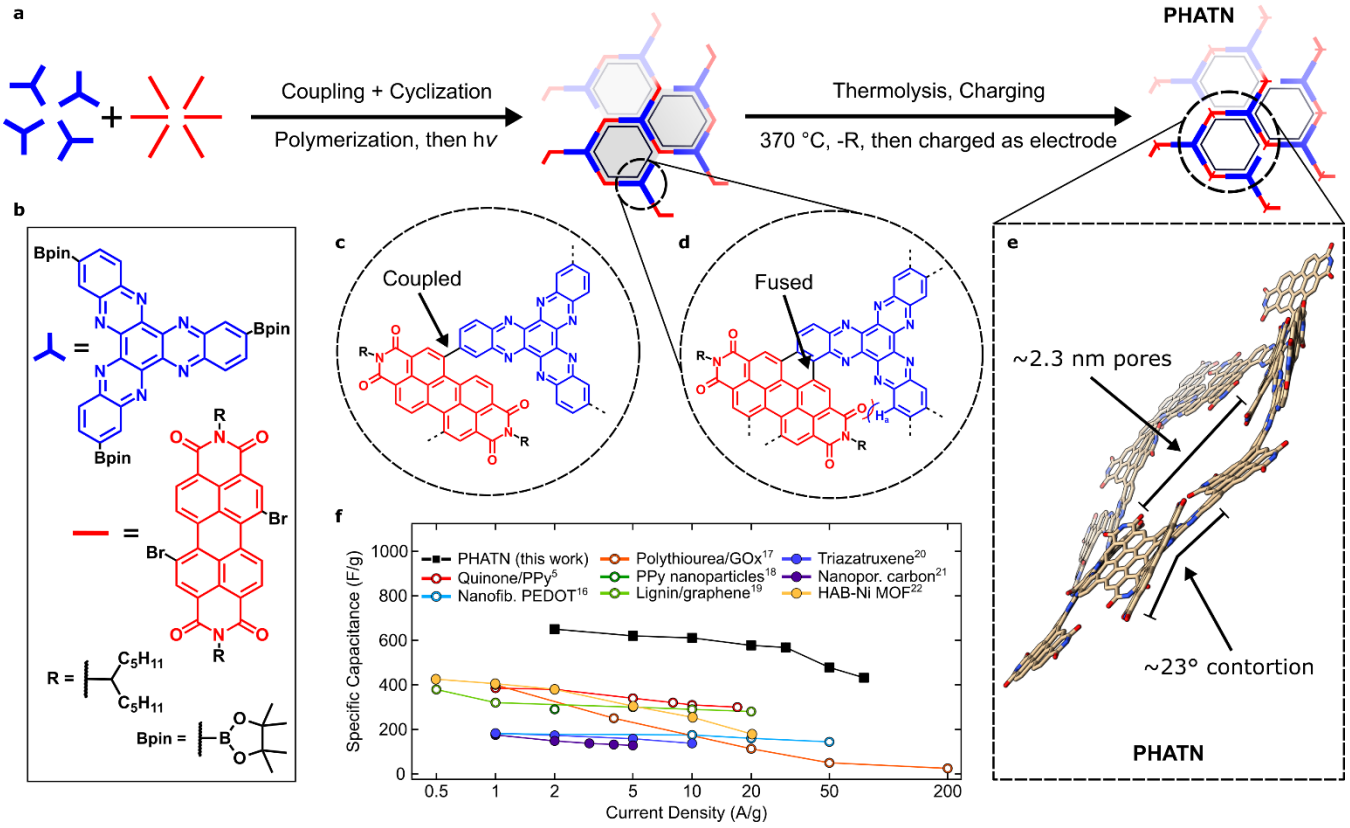

Fig. 1. Synthesis, structure, and performance of the electroactive polymer PHATN. a, Design employed in the fabrication of **PHATN**. Opacity offset indicates the three-dimensional nature of the helical network. **b**, Key for building blocks. **c**, PDI (red) is coupled to a three-pronged HATN scaffold (blue). **d**, The network is cyclized using a visible-light flow photocyclization

reaction. The resulting material is thermolyzed to free the electroactive polymer from the insulating alkyl chains. **e**, DFT representation of an idealized pore of **PHATN**, with an approximate idealized pore diameter of 2.3 nm. The calculated angle of contortion for this structure is ~23°. The material exhibits a contorted conformation due to steric hindrance from the imide position (see hydrogen labeled H_a in Fig. 1d). **f**, Specific capacitance (C_s) versus current density for **PHATN** (black) and other recent organic pseudocapacitor materials. Filled symbols represent negative electrode materials, and open symbols represent positive electrode materials. See references [5,16-22] for the compared systems and Extended Data Fig. 9 for a more comprehensive chart that includes a wider range of inorganic and hybrid materials.

To evaluate the electrochemical behavior of this new material, we fabricated working electrodes by drop casting onto carbon paper a slurry of **PHATN**, carbon black (as conductive agent) and polytetrafluoroethylene (as binder) in a mass ratio of 8:1:1 suspended in N-methyl-2-pyrrolidone. We utilized a three-electrode setup comprising the **PHATN** working electrode, a graphite counter electrode and a Hg/HgO reference electrode, all suspended in 6 M KOH aqueous electrolyte. The **PHATN** electrode was presoaked in electrolyte under vacuum to ensure full infiltration of the pores. During this process, the imide carbonyls associate with K^+ in solution, as indicated by a shift of the carbonyl ^{13}C ssNMR resonance to higher frequency upon soaking (Extended Data Fig. 1b). Note that the ^{13}C ssNMR chemical shift upon K^+ ion association is remarkably large, a consequence of the molecular contortion.[23,24] In addition, the contortion of **PHATN** produces easily accessible internal surface area, as demonstrated by the large Brunauer-Emmett-Teller (BET) surface area of 131 m^2/g calculated from gas adsorption isotherms collected using CO_2 (Extended Data Fig. 2). Together, the ^{13}C ssNMR and gas adsorption isotherm measurements support the contortion model and resulting pore infiltration hypothesis.

Cyclic voltammetry (CV) of the **PHATN** electrode reveals broad and overlapping reduction peaks at –0.7 and –1.0 V vs. Hg/HgO (Fig. 2a, b). These fully reversible peaks originate from the sequential reductions of the PDI and HATN units. To confirm this assignment, we investigated the individual redox processes by performing CV measurements of PDI, HATN and **PHATN monomer** in solution (Fig. 2c). Both PDI and HATN display two clear reduction peaks, with the HATN pair at slightly more negative potential.[11,25] The CV of **PHATN monomer** can be understood as a convolution of these two behaviors. These observations are supported by DFT of the **PHATN monomer**: the levels associated with the PDI moieties are more energetically accessible than those associated with the HATN moieties (Fig. 2d). Fig. 2e illustrates the charge storage mechanism of **PHATN**: the PDI moiety first accepts two electrons,[26] then the HATN moiety accepts two more.[11,27] The charges are delocalized across their respective π-systems, giving rise to the observed broad and overlapping peaks. This mechanism leads to a calculated theoretical specific capacitance of 996 F/g for **PHATN**.

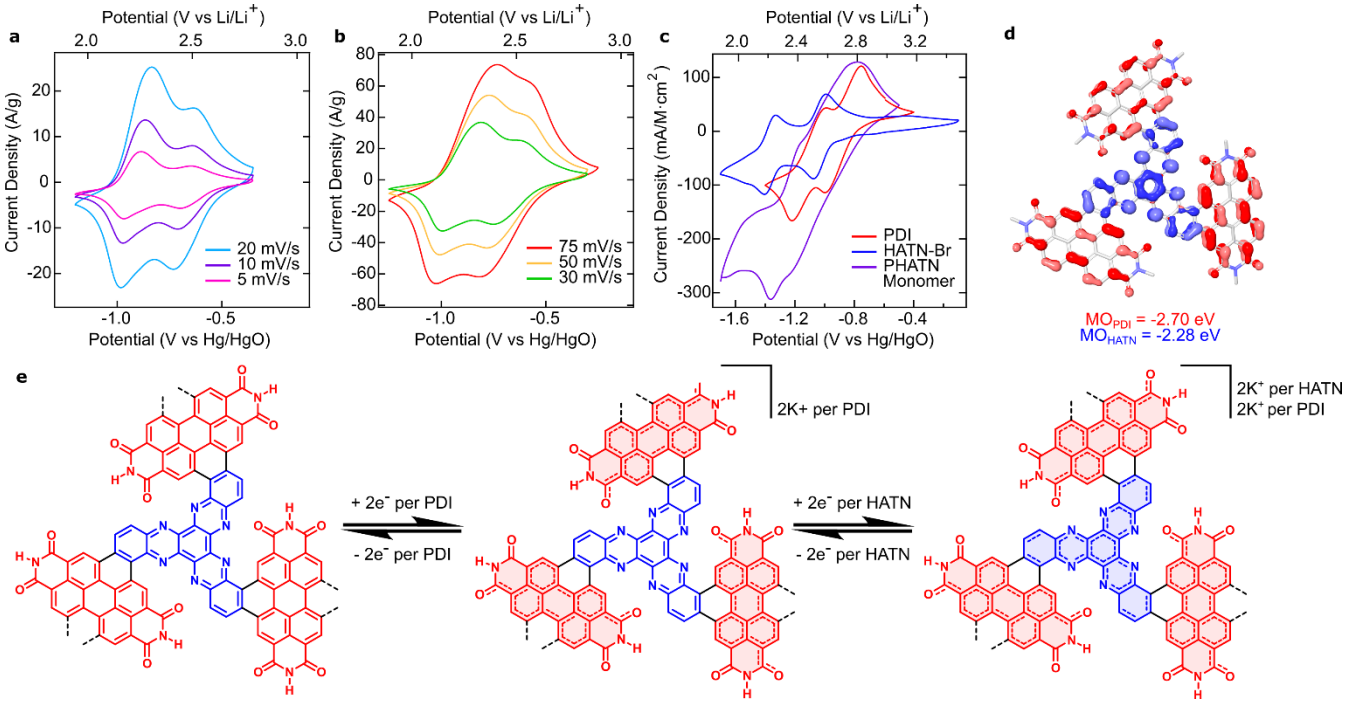

Fig. 2. **Three-electrode cyclic voltammetry and charging mechanism of PHATN. a**, Three-electrode CV of **PHATN** showing broad and reversible reduction peaks at low and **b**, high rates. The electrolyte is a 6 M KOH aqueous solution. **c**, Solution-phase CVs of individual **PHATN** building blocks show two distinct reductions each, overlapping with the **PHATN monomer**. The current densities of HATN-Br and **PHATN monomer** are scaled to match the concentration of PDI (0.01 M). The electrolyte is 0.1 M TBA-PF_6 in DCM. **d**, Unoccupied molecular orbital (MO) levels of the building blocks. Three degenerate MOs comprise the total PDI visualization, and a single MO comprises the HATN visualization. The PDI moieties are reduced before the HATN moieties. Lighter MOs indicate opposing phases. **e**, Proposed mechanism for charge storage within the extended **PHATN** system. Reversible reduction events store two electrons per PDI (red) followed by two electrons per HATN (blue).

To understand the remarkable charge storage kinetics of **PHATN** and demonstrate its capacitive behavior, we performed CV at different scan rates (1 to 300 mV/s). The reduction peaks display a slight anodic shift with respect to the oxidation peaks. When intercalation kinetics are at play in battery materials, this shift is often greater than 0.1 V, even at rates as low as 0.1 mV/s, and increases dramatically at higher rates,[28] leading to reduced energy efficiency. In contrast, pseudocapacitors are kinetically limited at low rates only by the speed of the surface-level Faradaic reactions (i.e. surface-controlled), and at higher rates by electrolyte diffusion. Fig. 3a shows the peak separation of the first redox event in **PHATN** as a function of sweep rate. At low rates, the peaks are nearly coincident (separation <0.05 V) and the separation increases slowly with sweep

rate, indicating surface-limited redox behavior.[28,29] Above a critical rate of ~50 mV/s, the peak shift increases more dramatically, as the system reaches diffusion-limited behavior.

Fig. 3b displays a log-log plot of the sweep rate (v) versus peak current (i). These parameters obey the power law given in Equation 1:

$$i \propto v^b \quad (1)$$

where the slope of the linear fit of the log-log plot is b. From the lowest rate up to 50 mV/s, the slope b of the linear fit is 0.98. A value near 1 indicates purely surface-controlled behavior, while $b = 0.5$ implies diffusion-controlled Randles-Sevcik behavior.[30] Above 50 mV/s, the slope decreases to 0.72, suggesting a rate limitation that arises from diffusion constraints. That the surface-controlled regime extends to such high rates supports the pseudocapacitive behavior and explains the exceptionally good performance of **PHATN** at fast charging speeds.

The relationship between capacity (Q) and sweep rate provides further evidence for surface-mediated charge storage in **PHATN**. Fig. 3c displays a plot of Q vs $v^{-1/2}$. Rates below 50 mV/s have purely surface-controlled kinetics, while higher sweep rates are limited by diffusion. By taking a linear extrapolation of this surface-controlled region to $v = \infty$, the infinite sweep rate capacity can be estimated, which corresponds to the "outer" charge of the material, i.e. easily accessible by the electrolyte.[31-33] Similarly, a plot of 1/Q vs $v^{1/2}$ (Fig. 3d) can be extrapolated to $v = 0$ to estimate the "total" charge, which includes areas shielded from electrolyte. Here, the outer charge is estimated at 105 mAh/g, representing 60% of the total charge, 174 mAh/g. This ratio indicates that a majority of the charge capacity of the material is found in electrolyte-accessible regions and is due to surface processes. Together, these results support rapid surface-level redox activity as the source of the material's high rate capability. As discussed below, this high rate capability is enabled by molecular contortion, which permits both long-range conjugation and highly accessible areas for redox activity.

Fig. 3e shows galvanostatic charge-discharge (GCD)[20] curves of the material in a three-electrode set-up, at current densities ranging from 0.5 to 2 A/g. The triangular shape characteristic of capacitor-like materials is obvious. We note that at lower currents, electrolysis of water begins to dominate the reduction cycle, lowering the coulombic efficiency. From the GCD data, we calculate specific capacitance with Equation 2:

$$C_s = \frac{I \cdot t}{\Delta E} \quad (2)$$

where I is current density, t is cycle time, and ΔE is the potential difference between the top and bottom of the cycle. At 0.5 A/g, we measure an extremely high capacitance of 689 F/g, far surpassing comparable organic pseudocapacitor materials, both negative and positive electrodes alike (Fig. 1f, Extended Data Fig. 9). This value is 69% of the theoretical capacitance (996

F/g), in agreement with the Q-*v* analysis, and suggesting that even better performance could be achieved with further device optimization and nanostructuring.[34] The capacitance decreases at higher cycling rates, as expected from the kinetic limitations detailed above, but even at the highest measured current density of 75 A/g, **PHATN** retains performance of 432 F/g (Supplementary Table 3).

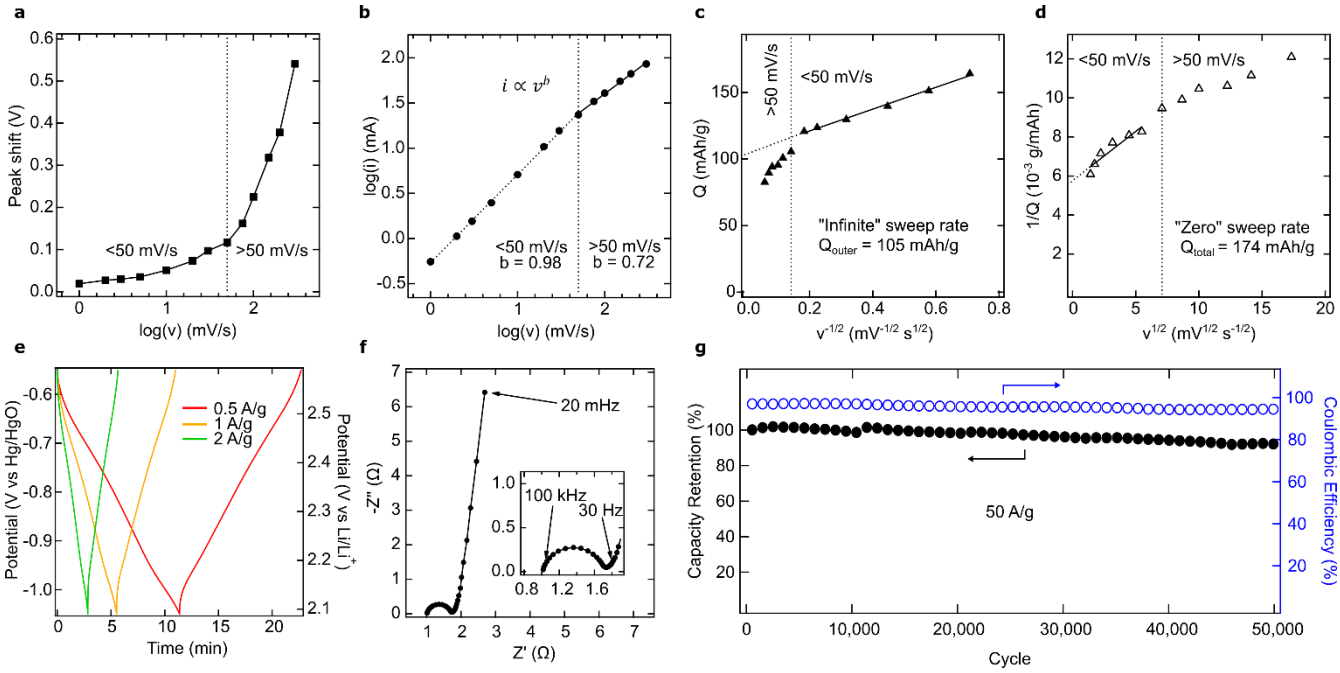

Fig. 3. **Three-electrode electrochemical characterization of pseudocapacitive behavior and kinetics of PHATN**. **a**, Anodic peak shift of the first redox couple at different sweep rates, showing small shift at rates below 50 mV/s. **b**, Log-log plot of peak current vs. sweep rate, showing a slope near 1 below 50 mV/s. **c**, Q vs $v^{-1/2}$, with extrapolation to v = ∞ to estimate the outer charge storage. **d**, 1/Q vs $v^{1/2}$, with extrapolation to v = 0 to estimate the total charge storage. **e**, Three-electrode GCD cycling of **PHATN** at different current densities exhibiting the triangular shape characteristic of pseudocapacitors. **f**, Nyquist plot from 100 kHz to 20 mHz shows a small semicircle at high frequency and a steep Warburg slope at low frequency. **g**, Cycling stability over 50,000 cycles at a current density of 50 A/g. The left axis (black, filled circles) displays capacity retention, and the right axis (blue, open circles) displays coulombic efficiency. Measurements in **a**-**g** were performed in 6 M KOH aqueous electrolyte.

We measured the impedance of the system at different frequencies (*f*) using electrochemical impedance spectroscopy (EIS). Fig. 3f displays the Nyquist plot of **PHATN** collected at –0.7 V vs. Hg/HgO. The high frequency region, from 100 kHz

to 30 Hz, shows a semicircular shape with a diameter of ~0.8 Ω, indicating very low interfacial charge-transfer resistance (R_{ct}).[35] The high frequency x-intercept of the curve represents the equivalent series resistance (ESR, R_s) of the entire system, ~1 Ω. Finally, the low frequency region corresponds to the Warburg impedance (Z_W), with the near-vertical slope indicating fast diffusion of ions towards the electrode surface. The specific capacitance as a function of frequency can also be calculated from EIS data using Equation 3.

$$C(f) = -\frac{1}{2\pi \cdot m \cdot Z'' \cdot f} \qquad (3)$$

A value of around 800 F/g is achieved at the lowest frequencies, while capacitance values of 400 F/g and 200 F/g are retained even at 1 Hz and 10 Hz, respectively (Extended Data Fig. 3c). We also tested the cycling stability of **PHATN** at a high current density of 50 A/g (Fig. 3g, Supplementary Fig. 10c) and observed an 8% decrease in capacitance and no decrease in coulombic efficiency over 50,000 cycles. Another device was cycled 10,000 times at 20 A/g, with 3% decrease in capacitance (Supplementary Fig. 10b). Self-discharge measurements show a behavior comparable to other organic supercapacitor materials, retaining 84% capacity after 3 hours (Extended Data Fig. 4). The retained capacity increases to 99% after 3 hours when the electrode is held at –1.0 V for 10 minutes before the self-discharge test.

To conclusively demonstrate the efficacy of the contortion design, we synthesized a planar analogue of **PHATN** composed of alternating phenazine and PDI units (**PA-PDI**). The synthesis and characterization of this control system are reported here for the first time. Phenazine emulates the structure and electrochemical properties of HATN, but, as opposed to the tritopic contorted HATN, it cyclizes with PDI to form a planar linear structure (Supplementary Scheme 6). The cyclic voltammogram of **PA-PDI** resembles that of **PHATN** (Extended Data Fig. 5a, 6a) but its capacitance is notably lower (e.g., 100 F/g at 10 A/g) (Extended Data Fig. 7a) and the shallower Warburg slope from EIS indicates a less capacitive behavior (Extended Data Fig. 6c). The cycling performances of **PA-PDI** and **PHATN** are comparable, underlining the general and outstanding stability of the structures produced by coupling PDI and annulated pyrazines (e.g. PA and HATN) (Extended Data Fig. 7b). The key difference is that the diffusion coefficient of ions in **PHATN** is almost one order of magnitude larger than in **PA-PDI**, as measured by the galvanostatic intermittent titration technique (Extended Data Fig. 8). Consistent with this result, gas adsorption isotherms in **PA-PDI** reveal much a smaller surface area (12 m^2/g) than in the contorted **PHATN** (Extended Data Fig. 2). Overall, we attribute these differences to the contortion of **PHATN**. Namely, (1) contortion improves accessible surface area[36] to facilitate ion diffusion, (2) contortion improves solubility by preventing π-π stacking during synthesis[14], which may in turn lead to larger molecular weight polymers, and (3) contortion enables cavity-like and bowl-like shape-matching for potential guest ions to easily bind in a stable and reversible fashion.[15]

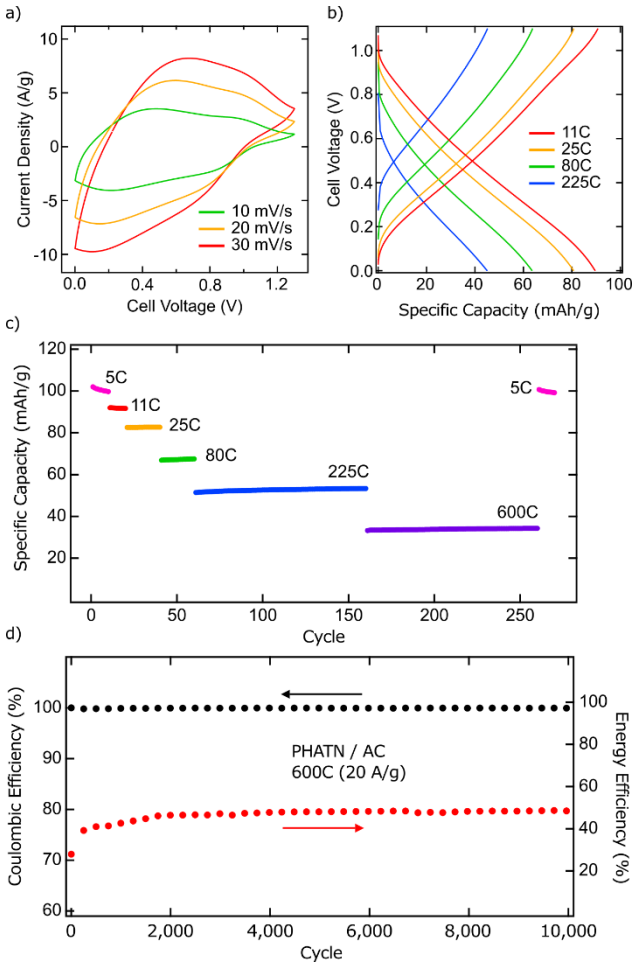

Fig. 4. Characterization of two-electrode button cells assembled from PHATN(–) and activated carbon(+) electrodes. **a**, CV of the device, showing overall rectangular shape and a suggestion of the two redox peaks characteristic of **PHATN**. **b**, Charge-discharge curves of the **PHATN** / AC cell showing substantial capacity, even at extremely high C-rates. **c**, Capacity retention of the **PHATN** / AC cell at sequentially higher rates. After GCD cycling up to an extremely high rate of 600C, the rate can be lowered back to 5C while maintaining the original capacity. **d**, Coulombic and energy efficiency of the **PHATN** / AC device over 10,000 cycles at a rate of 600C (20 A/g). Energy efficiency is low due to the relatively low voltage of the **PHATN** / AC cell. Measurements in **a-d** were performed using 6 M KOH aqueous electrolyte with a **PHATN** electrode mass loading of 6.4 mg/cm^2.

Taken together, the results presented here indicate that **PHATN** holds potential as a practical electrode material, leading us to further investigate its use in a realistic device architecture. Using **PHATN**, we constructed and tested two-electrode capacitor devices. We assembled several different architectures of two-electrode cells, using **PHATN** and activated carbon

(AC) as the negative and positive electrodes, respectively (full results in Supplementary Figs. 12-22, Supplementary Tables 5-7). To highlight the versatility of **PHATN** as a negative electrode, we also fabricated two-electrode "hybrid" devices using $Ni(OH)_2$ as the positive electrode, which shows similar performance to activated carbon (discussed in Supplementary Figs. 23-27). CV of the AC-based two-electrode cell produces a similar shape to that seen in the three-electrode measurements, with multiple broad overlapping peaks (Fig. 4a). While the contribution of the AC electrode causes some expected asymmetry between the cathodic and anodic peaks, the accessible voltage window is extended to 1.3 V, much higher than for the individual **PHATN** electrode.

Charge-discharge measurements (Fig. 4b) confirm that the high rate capability of **PHATN** is maintained in the two-electrode devices. At the lowest rate of 5 C (0.5 A/g), we measure a capacity of 103 mAh/g, slightly less than that found in the single electrode. Even at the extraordinarily high rate of 600C (20 A/g), the cell still displays a capacity of over 30 mAh/g and is able to return to lower rates without a loss in performance (Fig. 4c). Furthermore, the cell has good cycling stability at high rates, cycling 10,000 times at 600C with near 100% Coulombic efficiency (Fig. 4d) and no loss in capacity (Supplementary Fig. 15).

In summary, we have demonstrated a robust organic material composed of PDI and HATN exhibiting best-in-class energy storage properties among organic pseudocapacitor materials. Displaying single electrode capacitance of nearly 700 F/g in aqueous electrolyte and high performance at current densities of up to 75 A/g over tens of thousands of cycles, this system pushes the boundaries of organic energy storage materials. These properties are a direct consequence of our design principles: 1) the combination of complementary organic components which increase the total available energy and potential window, and 2) molecular contortion to permit both facile diffusion and long-range charge delocalization. Such characteristics combine synergistically to promote rapid charging, high capacitance, and long-term stability. Future designs could explore the use of larger polycyclic aromatic hydrocarbon fragments, such as coronene, decorated with electronically tunable edge groups and cyclized onto a three-pronged scaffold such as triptycene or hexaazatrinaphthylene. Taken together, these results advance our fundamental understanding of the design characteristics necessary to achieve high-performance pseudocapacitors, and underpin promising developments in the search for affordable, organic, high-power energy storage solutions.

References

1 Schmidt, O., Hawkes, A., Gambhir, A. & Staffell, I. The future cost of electrical energy storage based on experience rates. *Nat. Energy* **2**, 1-8, (2017).

2 Lu, Y. & Chen, J. Prospects of organic electrode materials for practical lithium batteries. *Nat. Rev. Chem.*, 1-16, (2020).

3 Pomerantseva, E., Bonaccorso, F., Feng, X., Cui, Y. & Gogotsi, Y. Energy storage: The future enabled by nanomaterials. *Science* **366**, eaan8285, (2019).

4 Choi, C. *et al.* Achieving high energy density and high power density with pseudocapacitive materials. *Nat. Rev. Mater.*, 1-15, (2019).

5 Kim, S. K., Cho, J., Moore, J. S., Park, H. S. & Braun, P. V. High-Performance Mesostructured Organic Hybrid Pseudocapacitor Electrodes. *Adv. Funct. Mater.* **26**, 903-910, (2016).

6 Boota, M. & Gogotsi, Y. MXene—conducting polymer asymmetric pseudocapacitors. *Adv. Energy Mater.* **9**, 1802917, (2019).

7 Bryan, A. M., Santino, L. M., Lu, Y., Acharya, S. & D'Arcy, J. M. Conducting polymers for pseudocapacitive energy storage. *Chem. Mater.* **28**, 5989-5998, (2016).

8 Faulkner, E. B. & Schwartz, R. J. *High performance pigments*. (John Wiley & Sons, 2009).

9 Lee, S. K. *et al.* Electrochemistry, spectroscopy and electrogenerated chemiluminescence of perylene, terrylene, and quaterrylene diimides in aprotic solution. *J. Am. Chem. Soc.* **121**, 3513-3520, (1999).

10 Geng, J., Renault, S., Poizot, P. & Dolhem, F. in *Energy Harvesting and Storage: Materials, Devices, and Applications II.* 803504 (International Society for Optics and Photonics).

11 Peng, C. *et al.* Reversible multi-electron redox chemistry of π-conjugated N-containing heteroaromatic molecule-based organic cathodes. *Nat. Energy* **2**, 1-9, (2017).

12 Peurifoy, S. R. *et al.* Three-dimensional graphene nanostructures. *J. Am. Chem. Soc.* **140**, 9341-9345, (2018).

13 Schuster, N. J. *et al.* Electron delocalization in perylene diimide helicenes. *Angew. Chem. Int. Ed.* **128**, 13717-13721, (2016).

14 Zhong, Y. *et al.* Helical ribbons for molecular electronics. *J. Am. Chem. Soc.* **136**, 8122-8130, (2014).

15 Peurifoy, S. R. *et al.* Dimensional Control in Contorted Aromatic Materials. *Chem. Rec.* **19**, 1050-1061, (2019).

16 Acharya, S. *et al.* Ultrahigh stability of high-power nanofibrillar PEDOT supercapacitors. *Sustain. Energ. Fuels* **1**, 482-491, (2017).

17 Witomska, S. *et al.* Graphene Oxide Hybrid with Sulfur–Nitrogen Polymer for High-Performance Pseudocapacitors. *J. Am. Chem. Soc.* **141**, 482-487, (2018).

18 Hou, Z., Yang, Q., Lu, H. & Li, Y. Towards enhanced electrochemical capacitance with self-assembled synthesis of poly (pyrrole-co-o-toluidine) nanoparticles. *J. Appl. Polym.* **133**, (2016).

19 Kim, S. K., Kim, Y. K., Lee, H., Lee, S. B. & Park, H. S. Superior Pseudocapacitive Behavior of Confined Lignin Nanocrystals for Renewable Energy-Storage Materials. *ChemSusChem* **7**, 1094-1101, (2014).

20 Li, X.-C. *et al.* Redox-active triazatruxene-based conjugated microporous polymers for high-performance supercapacitors. *Chem. Sci.* **8**, 2959-2965, (2017).

21 Park, S. K. *et al.* 105 cyclable pseudocapacitive Na-ion storage of hierarchically structured phosphorus-incorporating nanoporous carbons in organic electrolytes. *ACS Energy Lett.* **3**, 724-732, (2018).

22 Feng, D. *et al.* Robust and conductive two-dimensional metal− organic frameworks with exceptionally high volumetric and areal capacitance. *Nat. Energy* **3**, 30-36, (2018).

23 Forse, A. C., Griffin, J. M., Presser, V., Gogotsi, Y. & Grey, C. P. Ring current effects: factors affecting the NMR chemical shift of molecules adsorbed on porous carbons. *J. Phys. Chem. C* **118**, 7508-7514, (2014).

24 Cervini, L. *et al.* Factors affecting the nucleus-independent chemical shift in NMR studies of microporous carbon electrode materials. *Energy Storage Mater.* **21**, 335-346, (2019).

25 Matsunaga, T., Kubota, T., Sugimoto, T. & Satoh, M. High-performance lithium secondary batteries using cathode active materials of triquinoxalinylenes exhibiting six electron migration. *Chem. Lett.* **40**, 750-752, (2011).

26 Haeupler, B., Wild, A. & Schubert, U. S. Carbonyls: powerful organic materials for secondary batteries. *Adv. Energy Mater.* **5**, 1402034, (2015).

27 Hollas, A. *et al.* A biomimetic high-capacity phenazine-based anolyte for aqueous organic redox flow batteries. *Nat. Energy* **3**, 508-514, (2018).

28 Conway, B. E. Transition from "supercapacitor" to "battery" behavior in electrochemical energy storage. *J. Electrochem. Soc.* **138**, 1539, (1991).

29 Augustyn, V. *et al.* High-rate electrochemical energy storage through Li+ intercalation pseudocapacitance. *Nat. Mater.* **12**, 518-522, (2013).

30 Forghani, M. & Donne, S. W. Method comparison for deconvoluting capacitive and pseudo-capacitive contributions to electrochemical capacitor electrode behavior. *J. Electrochem. Soc.* **165**, A664-A673, (2018).

31 Ardizzone, S., Fregonara, G. & Trasatti, S. "Inner" and "outer" active surface of RuO2 electrodes. *Electrochim. Acta* **35**, 263-267, (1990).

32 Baronetto, D., Krstajić, N. & Trasatti, S. Reply to "note on a method to interrelate inner and outer electrode areas" by H. Vogt. *Electrochim. Acta* **39**, 2359-2362, (1994).
33 Lee, J.-S. M., Briggs, M. E., Hu, C.-C. & Cooper, A. I. Controlling electric double-layer capacitance and pseudocapacitance in heteroatom-doped carbons derived from hypercrosslinked microporous polymers. *Nano Energy* **46**, 277-289, (2018).
34 Lu, Q., Chen, J. G. & Xiao, J. Q. Nanostructured electrodes for high-performance pseudocapacitors. *Angew. Chem. Int. Ed.* **52**, 1882-1889, (2013).
35 Xu, J. *et al.* Facile synthesis of novel metal-organic nickel hydroxide nanorods for high performance supercapacitor. *Electrochim. Acta* **211**, 595-602, (2016).
36 McKeown, N. B. *et al.* Polymers of intrinsic microporosity (PIMs): bridging the void between microporous and polymeric materials. *Chem. Eur. J.* **11**, 2610-2620, (2005).

Methods:

Synthetic details:

All reactions were carried out under inert atmosphere using standard Schlenk techniques, unless otherwise noted. Dry and deoxygenated solvents were prepared by elution through a dual-column solvent system (Glass Contour).

1-bromoperylene-3,4,9,10-tetracarboxylicdiimide and a mixture of 1,6- and 1,7-dibromoperylene-3,4,9,10-tetracarboxylicdiimide were synthesized according to our reported procedures.[37] Tribromo hexaazatrinaphthylene (**HATN-Br**) was prepared according to a reported procedure[38] and used in the synthesis of **HATN-bpin**. **PA-dibpin**[39,40] was prepared according to reported procedures and used in the synthesis of **PA-PDI**. [1,1′-Bis(diphenylphosphino)ferrocene]dichloropalladium(II), potassium carbonate, cyclohexaneketone octahydrate, 4-bromobenzene-1,2-diamine, and bis(pinacolato)diboron were purchased from Millipore Sigma.

The flow reactor is a home-built reactor[41-43] consisting of a peristaltic pump (Masterflex L/S PTFE-Tubing Pump System; 3 to 300 rpm, 90 to 260 VAC; Item# UX-77912-10), FEP tubing (Chemfluor FEP tubing), and 17,500 lumen LED cornbulb lamps (EverWatt, EWIP64CB150WE39NB24, 150 W). The tubing was wrapped around the LED bulbs to provide the reaction surface. During the photocyclization reaction, the temperature was ~55-65 °C.

Synthesis of HATN-bpin:

A 100 mL oven-dried flask was charged with a stir bar, a regioisomeric mixture of tribromo hexaazatrinaphthylene (3.58 g, 5.76 mmol), bis(pinacolato)diboron (8.95 g, 35.4 mmol), $Pd(dppf)Cl_2$ (412 mg, 0.563 mmol), and potassium acetate (3390 mg, 34.6 mmol). The charged vial was capped with a rubber septum, evacuated and backfilled with N_2. Degassed dioxane (37.9 mL) was syringed into the flask. The mixture was then heated to 90 °C and stirred overnight. The solution was cooled to room temperature and diluted with dichloromethane, then dried. The crude mixture was dissolved in dichloromethane and filtered over a silica plug. This dark green solution was then dried again, brought up in a small amount of dichloromethane, and triturated into methanol. The suspension was washed over a Celite plug using methanol and a blue solution was pulled through using dichloromethane. This solution was dried to afford yellow-green solid hexaazatrinaphthylene tris-boronic acid pinacol ester (**HATN-bpin**) in 73% yield (3.2 g) consisting of a mixture of regioisomers. This regiomixture was carried forward through the following synthetic steps without further resolution. NMR provided (Supplementary Fig. 1, 2).

Synthesis of uncyclized PHATN:

A 20 mL vial was charged with a stir bar, **HATN-bpin** (460 mg, 0.6 mmol), a mixture of 1,6- and 1,7-dibromoperylene-3,4,9,10-tetracarboxylicdiimide (770 mg, 0.9 mmol), $Pd(dppf)Cl_2$ (88 mg, 0.120 mmol), and potassium carbonate (665 mg, 4.8

mmol). The charged vial was capped with a rubber septum, evacuated and backfilled with N_2. Degassed water (1.5 mL) and degassed tetrahydrofuran (6.0 mL) were syringed into the vial. The mixture was then heated to 57 °C and stirred overnight. The solution was cooled to room temperature and diluted with water and dichloromethane. The mixture was triturated with methanol, and the solid was collected. The solid was subjected to consecutive Soxhlet extractions comprised of methanol, hexanes, and chloroform. The chloroform fraction was collected and dried to yield **uncyclized PHATN** as a maroon solid in 61% yield (520 mg).

Synthesis of PHATN:

In a 100 mL round bottom flask, **uncyclized PHATN** (100 mg) and iodine (25 mg) were dissolved in chlorobenzene (65 mL). The mixture was stirred for 15 minutes and then irradiated for 72 h with visible light using the home-built reactor described above. The solvent was then removed under vacuum and the resulting solid was suspended in methanol and loaded onto a Celite plug. The solid was washed with methanol, hexanes, and acetonitrile and then redissolved in chloroform. The solvent was removed under vacuum to afford **cyclized PHATN** as an orange solid in 90% yield (90 mg). The NMR of **PHATN monomer** (Supplementary Fig. 3) was used to assign the conformation of the extended material. **2 (Cyclized PHATN)** (141 mg) was sealed in a borosilicate glass tube under vacuum. The tube was placed in a tube furnace, with one end of the tube sticking out of the furnace and the other end containing the solid in the middle of the furnace. The furnace was heated to 375 °C for 2 hours, over which time the material turned black and a clear, yellow liquid condensed at the cool end of the tube. The tube was opened and thermolyzed **PHATN** was collected as an orange-black solid in 63% yield (89 mg).

Synthesis of PHATN monomer:

(i.) A 3 mL vial was charged with a stir bar, **HATN-bpin** (92 mg, 0.12 mmol), 1-bromoperylene-3,4,9,10-tetracarboxylicdiimide (290 mg, 0.372 mmol), $Pd(dppf)Cl_2$ (22 mg, 0.03 mmol), and potassium carbonate (133 mg, 0.96 mmol). The vial was capped with a rubber septum, evacuated and backfilled with N_2. Degassed water (0.3 mL) and degassed tetrahydrofuran (1.2 mL) were syringed into the vial. The mixture was then heated to 57 °C and stirred overnight. The solution was cooled to room temperature and diluted with water and dichloromethane. The mixture was triturated with methanol, and the solid was collected. The solid was washed with water then subjected to consecutive Soxhlet extractions comprised of methanol, hexanes, and chloroform. The chloroform fraction was collected and dried to afford **uncyclized PHATN monomer** as a maroon solid in 64% yield (190 mg).

(ii.) In a 100 mL round bottom flask, **uncyclized PHATN monomer** (100 mg) and iodine (25 mg) were dissolved in chlorobenzene (65 mL). The mixture was stirred for 15 minutes and then irradiated for 72 h with visible light

using a home-built photoreactor. The solvent was then removed under vacuum and the resulting solid was suspended in methanol and loaded onto a Celite plug. The solid was washed with methanol, hexanes, and then redissolved in chloroform. The solvent was removed under vacuum to provide a regioisomeric mixture of **PHATN "monomer"** as an orange solid. The symmetric isomer could be isolated in small yield by preparatory TLC methods and was used for structural assignment by NMR (Supplementary Fig. 3, 4).

Synthesis of Uncyclized PA-PDI:

A 50 mL vial was charged with a stir bar, **PA-dibpin** (400 mg, 0.93 mmol), a mixture of 1,6- and 1,7-dibromoperylene-3,4,9,10-tetracarboxylicdiimide (720 mg, 0.93 mmol), $Pd(dppf)Cl_2$ (136 mg, 0.19 mmol), and potassium carbonate (1020 mg, 7.4 mmol). The charged vial was capped with a rubber septum, evacuated and backfilled with N_2. Degassed water (1.5 mL) and degassed tetrahydrofuran (6.0 mL) were added to the vial with a syringe. The mixture was then heated to 57 °C and stirred overnight. The solution was cooled to room temperature and reduced under vacuum. The mixture was triturated with methanol, and the solid was collected. The solid was subjected to consecutive Soxhlet extractions comprised of methanol, hexanes, and chloroform. The chloroform fraction was collected and dried to yield **uncyclized PA-PDI** as a purple-black solid in 83% yield (671 mg).

Synthesis of Cyclized PA-PDI:

In a 150 mL erlenmeyer flask, **uncyclized PA-PDI** (251 mg) and iodine (36 mg) were dissolved in a mixture of chlorobenzene (100 mL) and chloroform (20 mL). The mixture was stirred until completely dissolved then irradiated for 72 h with visible light using the home-built reactor described above. The solvent was then removed under vacuum and the resulting solid was suspended in methanol and isolated using vacuum filtration and washed using methanol. After collecting solid, any additional solvent was removed under vacuum to afford **cyclized PA-PDI** as a dark purple solid in 38% yield (96 mg). **2** (**Cyclized PA-PDI**) (96 mg) was sealed in a quartz tube under vacuum. The tube was placed in a tube furnace, with one end of the tube sticking out of the furnace and the other end containing the solid in the middle of the furnace. The furnace was heated to 375 °C for 2 hours, over which time the material turned black and a clear, yellow liquid condensed at the cool end of the tube. The tube was opened and thermolyzed **PA-PDI** was collected as a purple-black solid in 60% yield (58 mg).

NMR

^1H spectra were recorded on a Bruker AVANCE III 500 (500 MHz) spectrometer, and ^{13}C spectra were recorded on a Bruker AVANCE III 400SL (400 MHz) spectrometer. Chemical shifts for protons are reported in parts per million downfield from tetramethylsilane and are referenced to residual protium within the NMR solvent ($CDCl_3$: δ 7.26 or $C_2D_2Cl_4$: δ 6.00).

Solid-state NMR

ssNMR experiments were performed on a Bruker Avance NEO 600 MHz spectrometer equipped with a 1.6 mm HXY MAS (magic-angle spinning) Chemagnetics probehead operating at 599.37 MHz for ^{1}H and 150.71 MHz for ^{13}C. Samples were packed in 1.6 mm ZrO_2 rotors and sealed with Torlon caps for measurement. Prior to each set of experiments, the magic-angle was set using KBr. ^{1}H-^{13}C cross polarization (CP)-MAS measurements were performed with a Hartmann-Hahn match of 60 kHz with a ramped (90-100%) pulse on ^{1}H, a contact time of 3 ms, a recycle delay of 3 s, ^{1}H decoupling at 120 kHz using TPPM, and between 4k-27k scans (depending on sample). ^{1}H NMR was externally referenced to adamantane at 1.85 ppm,^{13}C NMR was referenced to adamantane at 38.5 ppm.

Thermogravimetric analysis

Thermogravimetric analysis (TGA) traces were collected on a TA Instruments TGA Q500 under nitrogen flow.

Infrared spectroscopy

IR spectra were collected on a Perkin Elmer Spectrum 400 FT-IR.

Gas adsorption measurements

Gas adsorption isotherms for pressures in the range 0–760 torr were measured by a volumetric method using a Micromeritics ASAP 2020 gas sorption analyzer. Measurements were collected on approximately 200 mg of sample, which was evacuated by heating at 150 °C with a ramp rate of 10 °C/min under dynamic vacuum for 3 hours. Free-space correction measurements were performed using ultrahigh purity He gas. Ultrahigh purity (99.999%) CO_2 was used for measurements. Isotherms of CO_2 collected at 195 K were measured in a dry ice/isopropanol bath. Oil-free vacuum pumps and oil-free pressure regulators were used for all measurements to prevent contamination of the samples during the evacuation process, or of the feed gases during the isotherm measurements.

Gas chromatography mass spectrometry

GCMS data were collected on an Agilent Technologies GC-MS consisting of a 7890B GC inlet, 5977B mass spectrometer (electron impact ionization, EI), and a PAL LSI 85 autosampler.

Powder X-ray diffraction

PXRD patterns were measured on a PANalytical XPert3 Powder X-ray diffractometer, on a rotating Si zero-background plate.

Electrochemical Characterization:

Electrochemical measurements, including CV, GCD, and EIS, were performed on a Bio-Logic VSP-300 potentiostat/galvanostat running EC-lab software.

Solution-phase CV

The molecule of interest (**PDI**, **HATN-Br** or **PHATN monomer**) was dissolved to known concentration (0.01, 0.001, or 0.005 M, respectively) in a solution of DCM with 0.1 M tetrabutylammonium hexafluorophosphate ($TBAPF_6$) as supporting electrolyte. A three-electrode set-up was used with a 3 mm glassy carbon disc or 1.6 mm Pt disc as the working electrode, platinum wire as counter electrode, and a non-aqueous reference electrode composed of 0.01 M $Ag/AgNO_3$ in acetonitrile. Measurements were performed in a glovebox under N_2 atmosphere. The potential was swept from open circuit voltage to -1.7 V at rates ranging from 10 mV/s to 200 mV/s.

No difference was observed between glassy carbon and Pt working electrodes after correcting for electrode area. The glassy carbon electrode was used for subsequent measurements.

Peak current (i) from the cathodic trace of each scan was plotted vs the square root of sweep rate (v) (Supplementary Fig. 9). The resulting linear shape for each molecule indicates that each diffuses freely in solution without adsorption to the electrode, according to the Randles-Sevcik equation:

$$i = 0.446nFAC^0\sqrt{\frac{nFvD_0}{RT}}$$

where n is the number of electrons transferred, F is Faraday's constant, A is the surface area of the electrode, C^0 is the molecule concentration, and D_0 is the diffusion coefficient of the reduced molecule.

Electrode fabrication

The active material was ground in an agate mortar and pestle. The material was combined with carbon black and polytetrafluoroethylene (60% w/v suspension in water) in an 80/10/10 mass ratio. Approximately 3.6 times the total mass of the mixture was then added of n-methyl-2-pyrrolidone (NMP) to form a slurry. The slurry was stirred for several hours. Carbon paper (AvCarb MGL190) was cut into rectangles (~0.5-1 cm by 1-2 cm) and the resulting substrates were sonicated in 1 M H_2SO_4 for 20 min to remove any residue or carbon dust. The substrates were then washed with DI water and acetone, dried at 60 °C under vacuum, and weighed on an analytical balance (0.001 mg precision). The slurry was manually deposited on the bottom half of the substrates and pressed using a spatula. The electrode was dried at 70 °C under vacuum overnight. The electrode was then weighed on an analytical balance to obtain the active material mass. Typically, the mass loading was

2-3 mg/cm^2. Finally, prior to testing, the electrode was soaked in 6 M aqueous KOH solution under static vacuum for several hours.

Three-electrode measurements

Unless otherwise noted, measurements were performed in 6 M aqueous KOH electrolyte prepared from ultra-pure distilled water. Compared with organic electrolytes, the aqueous electrolyte has higher conductivity and may provide lower viscosity for faster ion diffusion through the material. Measurements were performed in a three-electrode cell with ~20 mL of electrolyte. A copper clip was used to hold the carbon paper working electrode, with a small piece of Ti foil interposed to prevent contact with electrolyte. The counter electrode was a graphite rod, and the reference was a Hg/HgO reference electrode in 6 M KOH (BASInc). Prior to measurement the electrolyte was sparged for 10 minutes with N_2 and the cell was subsequently kept under a blanketing N_2 atmosphere.

Cyclic voltammetry was performed in the range -1.25 to -0.3 V vs Hg/HgO, at rates from 1 to 300 mV/s. Galvanostatic charge-discharge measurements were performed by applying a constant current, with the current switching signs upon reaching set voltage limits of -1.15 and -0.65 V. The set current density was calculated using the equation:

$$I = \frac{i}{m_a}$$

where I is the current density, ranging from 0.5 to 75 A/g, i is the current, and m_a is the mass of active material. Unless stated otherwise, potentiostatic electrochemical impedance spectroscopy measurements were performed at -0.7 V vs Hg/HgO, in the frequency range 100 kHz to 20 mHz with a sinus amplitude of 5 mV.

Peak current potentials for cathodic shift (Fig. 3a) and *i*-*v* plots (Fig. 3b) were found with the EC-lab peak finding function and were taken from the first reduction peak (~ -0.7 V). Capacity for capacity vs. rate plots (Fig. 3c, d) was found by integrating under the CV curve.

Calculation of specific and volumetric capacitance

Specific capacitance via GCD:

$$C_s = \frac{i \cdot t}{m_a \cdot \Delta E}$$

where i is the current, t is the cycle time, m_a is the measured mass of the active material, and ΔE is the change in potential between the voltage limits.

Via EIS, series model:

$$C_s = \frac{-1}{Z'' \cdot 2\pi \cdot f}$$

where Z'' is the imaginary component of the resistance, and f is the EIS frequency.

Volumetric capacitance:

30 mg **PHATN** was pressed into a circular pellet under 4 tons and measured (1.1 mm thick, 5 mm diameter). The resulting volume (21.6 mm^3) was used to calculate the density of **PHATN** (1.39 g/cm^3). This density multiplied by specific capacitance gives volumetric capacitance.

Potential-dependent EIS

The potential was held for 1 minute. Then, a sinusoidal potential was applied with 5 mV amplitude and frequencies ranging from 100 kHz to 20 mHz.

Characterization in organic electrolyte

The supporting electrolyte was 0.1 M tetraethylammonium hexafluorophosphate (TEA-PF_6), the counter electrode was a platinum mesh, and the non-aqueous reference electrode was 0.01 M $AgNO_3$ in acetonitrile. Measurements were performed in a glovebox under N_2 atmosphere.

Diffusion coefficient

The chemical diffusion coefficient, *D*, can be estimated from the GITT data using the equation[44]

$$D = \frac{4}{\pi * \tau} * \left(\frac{m * \rho}{S}\right)^2 * \left(\frac{\Delta V_S}{\Delta V_T}\right)^2$$

where τ is the current pulse length, m is the mass of the active material on the electrode, ρ is the density of the active material, S is the surface area of the electrode, ΔV_S is the change in steady state potential after each current pulse, and ΔV_T is the change in potential during the current pulse.

Two-electrode measurements

Two-electrode cells consisted of one **PHATN** electrode and one counter electrode, assembled into one of three different cell types: button cell, small pouch cell, and large pouch cell. The **PHATN** electrodes were fabricated as described above, using carbon paper (AvCarb MGL190) as the current collector.

Counter electrode fabrication

Two types of counter electrodes were fabricated:

1. Activated Carbon (AC) counter electrode: The AC was prepared using the alkali activation method.[45] Briefly, an apricot pit produced from north China was used as the starting material. The apricot pit was heated to 550 ºC and

pyrolyzed for 1 h in a tubular furnace under nitrogen (99.999%). The resulting char and potassium hydroxide were mixed with a weight ratio of 1:2 and heated to 700 ºC under nitrogen for 2 h to activate the material. After activation, the product was sequentially washed with 0.5 M HCl, hot water, and distilled water to remove the residual base completely, followed by drying at 120 ºC for 12 h, to get the final activated carbon sample. A mixture of 87 wt.% AC, 10 wt.% of acetylene black (Jinpu Co., Ltd. China) and 3 wt.% of PTFE binder (Shanghai Macklin Co., Ltd. China) was prepared and hot pressed into sheets with a thickness of ~0.35 mm as supercapacitor electrodes. Mass loading was 11 mg/cm^2.

2. $Ni(OH)_2$ counter electrode: A $Ni(OH)_2$ electrode was extracted from a discharged commercial Ni-metal hydride battery and cut into a 1 × 1 cm^2 square. The material was scraped off one face of the electrode. Mass loading (wet) of $Ni(OH)_2$ was around 100 mg/cm^2.

Button cell assembly

Two-electrode button cells were assembled according to established protocols.[46] Briefly, a circular **PHATN** electrode (1.27 cm diameter) was fabricated as described above. Mass loading was 6.4 mg/cm^2. This electrode was stacked with a cellulose filter paper separator (Whatman Grade 1, thickness = 180 μm) and an AC electrode (1.27 cm diameter, fabrication described above) and wet with 250 μL of 6 M KOH aqueous electrolyte (31 μL/mg active material). A steel spacer and spring were then added, and the stack was enclosed in a steel button cell shell and sealed with Parafilm to prevent electrolyte evaporation. The cell was then tested using a standard spring-loaded clip connected to the potentiostat. See Supplementary Fig. 13.

Small pouch cell assembly

Square electrodes with 1 cm^2 area were prepared as described above, with ~2 mg/cm^2 mass loading of **PHATN**. Activated carbon (see above) was used as the counter electrode. The two electrodes were separated with cellulose filter paper separator (Whatman Grade 1, thickness = 180 μm) and wetted with 300 μL of 6 M KOH aqueous electrolyte. The stack was placed inside a plastic pouch (~5 × 5 cm), contacted with Ti foil strips as current collectors (thickness ~0.13 mm), and sealed using an impulse heat sealer. No pressure or calendering was applied during sealing. The cell was clamped in a vice with flat blocks on either side to ensure good contact between all components, under a pressure of ~100 psi. The cell was then connected to the potentiostat. See Supplementary Fig. 16.

Large pouch cell assembly

Square electrodes of 10 cm^2 area were prepared with 6.7 mg/cm^2 mass loading of **PHATN**. Activated carbon (see above) was used as the counter electrode. The two electrodes were separated with cellulose filter paper separator (Whatman Grade 1, thickness = 180 μm) and wetted with 750 μL of 6 M KOH aqueous electrolyte (11 μL/mg active material). The stack was placed inside a plastic pouch (~4 x 4 cm), contacted with Ti foil strips as current collectors (thickness ~0.13 mm), and sealed under vacuum using a vacuum heat sealer. The cell was clamped in a vice with flat blocks on either side to ensure good contact between all components, under a pressure of ~100 psi. The cell was then connected to the potentiostat. See Supplementary Fig. 21.

Calculation of specific capacity, energy, and power

The specific capacity, energy, and power for the two-electrode cells were calculated from GCD data (discharge cycle). The specific capacity is calculated using the equation

$$Q_s = \frac{i \cdot t}{m_a}$$

where i is the current, t is the cycle time, and m_a is the mass of active material (**PHATN**) on the anode.

For calculating specific energy and power of the two-electrode cell, we use the total mass of all cell components, as is typical in the literature.[47,48] Specific energy is calculated using the equation

$$E_s = \frac{i \cdot t \cdot \Delta E}{m_{total}}$$

where ΔE is the change in potential, and m_{total} is given by

$$m_{total} = m_a + m_c + m_e$$

where m_c is the theoretical mass of $Ni(OH)_2$ or AC required to balance the measured discharge Q or C, respectively. For $Ni(OH)_2$ this is based on the theoretical capacity of $Ni(OH)_2$ (289.04 mAh/g), while for AC this is based on the reported capacitance of the AC material used (339 F/g).[45] m_e is the theoretical mass of electrolyte required to supply ions for the measured discharge Q.

Specific power was calculated using the equation

$$P_s = \frac{i \cdot \Delta E}{m_{total}}$$

Computational modeling

Quantum chemical calculations were performed using Jaguar 8.7, Schrodinger, Inc., New York, NY, 2013.[49] Geometries were optimized using the B3LYP or M06-2X functional and the 6-31G** basis set. The geometry of **PHATN monomer** is presented below as a rough electronic approximation of the geometry of the extended material **PHATN**.

Data availability:

The data that support the findings of this study are available from the corresponding authors upon reasonable request.

References:

37 Rajasingh, P., Cohen, R., Shirman, E., Shimon, L. J. & Rybtchinski, B. Selective bromination of perylene diimides under mild conditions. *J. Org. Chem.* **72**, 5973-5979 (2007).

38 Wang, J., Lee, Y., Tee, K., Riduan, S. N. & Zhang, Y. A nanoporous sulfur-bridged hexaazatrinaphthylene framework as an organic cathode for lithium ion batteries with well-balanced electrochemical performance. *Chem. Commun.* **54**, 7681-7684 (2018).

39 Yu, W. *et al.* Discovery of fused tricyclic core containing HCV NS5A inhibitors with pan-genotype activity. *Bioorg. Med. Chem. Lett.* **26**, 3158-3162 (2016).

40 Vitaku, E. *et al.* Phenazine-Based Covalent Organic Framework Cathode Materials with High Energy and Power Densities. *J. Am. Chem. Soc.* **142**, 16-20 (2019).

41 Sisto, T. J. *et al.* Long, atomically precise donor–acceptor cove-edge nanoribbons as electron acceptors. *J. Am. Chem. Soc.* **139**, 5648-5651 (2017).

42 Peurifoy, S. R. *et al.* Three-dimensional graphene nanostructures. *J. Am. Chem. Soc.* **140**, 9341-9345 (2018).

43 Peurifoy, S. R. *et al.* Designing three-dimensional architectures for high-performance electron accepting pseudocapacitors. *J. Am. Chem. Soc.* **140**, 10960-10964 (2018).

44 Shen, Z., Cao, L., Rahn, C. D. & Wang, C.-Y. Least squares galvanostatic intermittent titration technique (LS-GITT) for accurate solid phase diffusivity measurement. *J. Electrochem. Soc.* **160**, A1842 (2013).

45 Xu, B. *et al.* Activated carbon with high capacitance prepared by NaOH activation for supercapacitors. *Mater. Chem. Phys.* **124**, 504-509 (2010).

46 Muench, S. *et al.* Polymer-based organic batteries. *Chem. Rev.* **116**, 9438-9484 (2016).

47 Li, H. *et al.* A High-Performance Sodium-Ion Hybrid Capacitor Constructed by Metal–Organic Framework–Derived Anode and Cathode Materials. *Adv. Energy Mater.* **28**, 1800757 (2018).

48 Zheng, J. P. The limitations of energy density of battery/double-layer capacitor asymmetric cells. *J. Electrochem. Soc.* **150**, A484 (2003).

49 Bochevarov, A. D. *et al.* Jaguar: A high-performance quantum chemistry software program with strengths in life and materials sciences. *Int. J. Quantum Chem.* **113**, 2110-2142 (2013).

50 Mathis, T. S. *et al.* Energy storage data reporting in perspective—guidelines for interpreting the performance of electrochemical energy storage systems. *Adv. Energy Mater.* **9**, 1902007 (2019).

51 Yeager, H. & Steck, A. Cation and water diffusion in Nafion ion exchange membranes: influence of polymer structure. *J. Electrochem. Soc.* **128**, 1880 (1981).

52 Splith, T., Fröhlich, D., Henninger, S. K. & Stallmach, F. Development and application of an exchange model for anisotropic water diffusion in the microporous MOF aluminum fumarate. *J. Mag. Res.* **291**, 40-46 (2018).

53 Park, S. K. *et al.* 105 cyclable pseudocapacitive Na-ion storage of hierarchically structured phosphorus-incorporating nanoporous carbons in organic electrolytes. *ACS Energy Lett.* **3**, 724-732 (2018).

54 Lee, S. W. *et al.* High-power lithium batteries from functionalized carbon-nanotube electrodes. *Nat. Nanotechnol.* **5**, 531-537 (2010).

55 Zeng, L. *et al.* Carbonaceous mudstone and lignin-derived activated carbon and its application for supercapacitor electrode. *Surf. Coat. Technol.* **357**, 580-586 (2019).

56 Su, X.-L. *et al.* Three-dimensional porous activated carbon derived from loofah sponge biomass for supercapacitor applications. *Appl. Surf. Sci.* **436**, 327-336 (2018)

57 Witomska, S. *et al.* Graphene Oxide Hybrid with Sulfur–Nitrogen Polymer for High-Performance Pseudocapacitors. *J. Am. Chem. Soc.* **141**, 482-487 (2018).

58 Wang, Y., Tao, S., An, Y., Wu, S. & Meng, C. Bio-inspired high performance electrochemical supercapacitors based on conducting polymer modified coral-like monolithic carbon. *J. Mater. Chem. A* **1**, 8876-8887 (2013).

59 Kim, M., Lee, C. & Jang, J. Fabrication of highly flexible, scalable, and high-performance supercapacitors using polyaniline/reduced graphene oxide film with enhanced electrical conductivity and crystallinity. *Adv. Funct. Mater.* **24**, 2489-2499 (2014).

60 Kim, S. K., Kim, Y. K., Lee, H., Lee, S. B. & Park, H. S. Superior Pseudocapacitive Behavior of Confined Lignin Nanocrystals for Renewable Energy-Storage Materials. *ChemSusChem* **7**, 1094-1101 (2014).

61 Milczarek, G. & Inganäs, O. Renewable cathode materials from biopolymer/conjugated polymer interpenetrating networks. *Science* **335**, 1468-1471 (2012).

62 Li, X.-C. *et al.* Redox-active triazatruxene-based conjugated microporous polymers for high-performance supercapacitors. *Chem. Sci.* **8**, 2959-2965 (2017).
63 Kim, S. K., Cho, J., Moore, J. S., Park, H. S. & Braun, P. V. High-Performance Mesostructured Organic Hybrid Pseudocapacitor Electrodes. *Adv. Funct. Mater.* **26**, 903-910 (2016).
64 Hou, Z., Yang, Q., Lu, H. & Li, Y. Towards enhanced electrochemical capacitance with self-assembled synthesis of poly (pyrrole-co-o-toluidine) nanoparticles. *J. Appl. Polym.* **133** (2016).
65 Bachman, J. C. *et al.* Electrochemical polymerization of pyrene derivatives on functionalized carbon nanotubes for pseudocapacitive electrodes. *Nat. Commun.* **6**, 1-9 (2015).
66 Li, M. & Yang, L. Intrinsic flexible polypyrrole film with excellent electrochemical performance. *J. Mater. Sci.: Mater. Electron* **26**, 4875-4879 (2015).
67 Grover, S. *et al.* Polyaniline all solid-state pseudocapacitor: role of morphological variations in performance evolution. *Electrochim. Acta* **196**, 131-139 (2016).
68 Acharya, S. *et al.* Ultrahigh stability of high-power nanofibrillar PEDOT supercapacitors. *Sustain. Energ. Fuels* **1**, 482-491 (2017).
69 Su, D., Zhang, J., Dou, S. & Wang, G. Polypyrrole hollow nanospheres: stable cathode materials for sodium-ion batteries. *Chem. Commun.* **51**, 16092-16095 (2015).
70 Cong, H.-P., Ren, X.-C., Wang, P. & Yu, S.-H. Flexible graphene–polyaniline composite paper for high-performance supercapacitor. *Energy Environ. Sci.* **6**, 1185-1191 (2013).
71 Cai, Z. *et al.* Flexible, weavable and efficient microsupercapacitor wires based on polyaniline composite fibers incorporated with aligned carbon nanotubes. *J. Mater. Chem. A* **1**, 258-261 (2013).
72 Shen, K. *et al.* Supercapacitor electrodes based on nano-polyaniline deposited on hollow carbon spheres derived from cross-linked co-polymers. *Synth. Met* **209**, 369-376 (2015).
73 Wang, S. *et al.* Free-standing 3D graphene/polyaniline composite film electrodes for high-performance supercapacitors. *J. Power Sources* **299**, 347-355 (2015).
74 Sun, H. *et al.* A self-standing nanocomposite foam of polyaniline@ reduced graphene oxide for flexible super-capacitors. *Synth. Met.* **209**, 68-73 (2015).
75 Wang, Z., Tammela, P., Zhang, P., Strømme, M. & Nyholm, L. High areal and volumetric capacity sustainable all-polymer paper-based supercapacitors. *J. Mater. Chem. A* **2**, 16761-16769 (2014).
76 Gupta, A. K., Saraf, M., Bharadwaj, P. K. & Mobin, S. M. Dual Functionalized CuMOF-Based Composite for High-Performance Supercapacitors. *Inorg. Chem.* **58**, 9844-9854, doi:10.1021/acs.inorgchem.9b00909 (2019).
77 Chen, G.-F., Liu, Z.-Q., Lin, J.-M., Li, N. & Su, Y.-Z. Hierarchical polypyrrole based composites for high performance asymmetric supercapacitors. *J. Power Sources* **283**, 484-493 (2015).
78 Feng, D. *et al.* Robust and conductive two-dimensional metal−organic frameworks with exceptionally high volumetric and areal capacitance. *Nat. Energy* **3**, 30-36 (2018).
79 Jagadale, A. D. *et al.* Cobalt hydroxide [Co(OH)2] loaded carbon fiber flexible electrode for high performance supercapacitor. *RSC Adv.* **5**, 56942-56948 (2015).
80 Wang, H., Casalongue, H. S., Liang, Y. & Dai, H. Ni(OH)2 Nanoplates Grown on Graphene as Advanced Electrochemical Pseudocapacitor Materials. *J. Am. Chem. Soc.* **132**, 7472-7477 (2010).
81 Li, L., Chen, L., Qian, W., Xie, F. & Dong, C. Directly Grown Multiwall Carbon Nanotube and Hydrothermal MnO2 Composite for High-Performance Supercapacitor Electrodes. *Nanomaterials* **9**, 703 (2019).
82 Zhang, F. *et al.* A high-performance supercapacitor-battery hybrid energy storage device based on graphene-enhanced electrode materials with ultrahigh energy density. *Energy Environ. Sci.* **6**, 1623-1632 (2013).
83 Ma, H. *et al.* Disassembly–Reassembly Approach to RuO2/Graphene Composites for Ultrahigh Volumetric Capacitance Supercapacitor. *Small* **13**, 1701026 (2017).
84 Wang, Y. *et al.* Ultrathin NiCo-MOF Nanosheets for High-Performance Supercapacitor Electrodes. *ACS Appl. Energy Mater.* **2**, 2063-2071 (2019).
85 Zhai, T. *et al.* Phosphate Ion Functionalized Co3O4 Ultrathin Nanosheets with Greatly Improved Surface Reactivity for High Performance Pseudocapacitors. *Adv. Mater.* **29**, 1604167 (2017).
86 Sun, X. *et al.* Fabrication of PANI-coated honeycomb-like MnO2 nanospheres with enhanced electrochemical performance for energy storage. *Electrochim. Acta* **180**, 977-982 (2015).
87 Sun, M. *et al.* In situ growth of burl-like nickel cobalt sulfide on carbon fibers as high-performance supercapacitors. *J. Mater. Chem. A* **3**, 1730-1736 (2015).
88 Zhou, J. *et al.* Importance of polypyrrole in constructing 3D hierarchical carbon nanotube@MnO2 perfect core–shell nanostructures for high-performance flexible supercapacitors. *Nanoscale* **7**, 14697-14706, doi:10.1039/C5NR03426D (2015).
89 Zhang, X., Ji, L., Zhang, S. & Yang, W. Synthesis of a novel polyaniline-intercalated layered manganese oxide nanocomposite as electrode material for electrochemical capacitor. *J. Power Sources* **173**, 1017-1023 (2007).
90 Li, L. *et al.* Facile Synthesis of MnO2/CNTs Composite for Supercapacitor Electrodes with Long Cycle Stability. *J. Phys. Chem. C* **118**, 22865-22872, doi:10.1021/jp505744p (2014).
91 Liu, Z., Xu, K., Sun, H. & Yin, S. One-Step Synthesis of Single-Layer MnO2 Nanosheets with Multi-Role Sodium Dodecyl Sulfate for High-Performance Pseudocapacitors. *Small* **11**, 2182-2191, doi:10.1002/smll.201402222 (2015).

92 Liang, Y. *et al.* Direct Access to Metal or Metal Oxide Nanocrystals Integrated with One-Dimensional Nanoporous Carbons for Electrochemical Energy Storage. *J. Am. Chem. Soc.* **132**, 15030-15037, doi:10.1021/ja106612d (2010).
93 Rajagopal, R., Lee, Y. S. & Ryu, K.-S. Synthesis and electrochemical analysis of Nb2O5-TiO2/H-rGO sandwich type layered architecture electrode for supercapacitor application. *Chem. Eng.* **325**, 611-623 (2017).
94 Seok, J. Y., Lee, J. & Yang, M. Self-Generated Nanoporous Silver Framework for High-Performance Iron Oxide Pseudocapacitor Anodes. *ACS Appl. Mater. Interfaces* **10**, 17223-17231, doi:10.1021/acsami.8b03725 (2018).
95 Pan, Z. *et al.* In Situ Growth of Layered Bimetallic ZnCo Hydroxide Nanosheets for High-Performance All-Solid-State Pseudocapacitor. *ACS Nano* **12**, 2968-2979, doi:10.1021/acsnano.8b00653 (2018).
96 Pang, H. *et al.* Cu superstructures fabricated using tree leaves and Cu–MnO2 superstructures for high performance supercapacitors. *J. Mater. Chem. A* **1**, 5053-5060, doi:10.1039/C3TA10523G (2013).
97 Ding, K., Zhang, X., Li, J., Yang, P. & Cheng, X. Phase and morphology evolution of ultrathin Co(OH)2 nanosheets towards supercapacitor application. *CrystEngComm* **19**, 5780-5786, doi:10.1039/C7CE01130J (2017).
98 Song, Y. *et al.* A polyanionic molybdenophosphate anode for a 2.7 V aqueous pseudocapacitor. *Nano Energy* **65**, 104010 (2019).
99 Chen, H. *et al.* One-Step Fabrication of Ultrathin Porous Nickel Hydroxide-Manganese Dioxide Hybrid Nanosheets for Supercapacitor Electrodes with Excellent Capacitive Performance. *Adv. Energy Mater.* **3**, 1636-1646, doi:10.1002/aenm.201300580 (2013).
100 Qiu, K. *et al.* Mesoporous, hierarchical core/shell structured ZnCo2O4/MnO2 nanocone forests for high-performance supercapacitors. *Nano Energy* **11**, 687-696 (2015).
101 Wu, M.-S. & Wu, J.-F. Nickel hydroxide electrode with porous nanotube arrays prepared by hydrolysis and cathodic deposition for high-performance supercapacitors. *J. Power Sources* **240**, 397-403 (2013).
102 Soltanloo, M., Kazazi, M., Yeganeh, S. E. H., Chermahini, M. D. & Mazinani, B. High-Performance Pseudocapacitive Electrode Based on Electrophoretically Deposited NiCo2O4/MWCNTs Nanocomposite on 316L Stainless Steel. *JOM* **72**, 2235-2244, doi:10.1007/s11837-020-04082-y (2020).
103 Liu, X. *et al.* Multi-shelled Ni 6 MnO 8 hollow microspheres for high-performance supercapacitors. *Mater. Res. Express* (2020).
104 Yang, G.-W., Xu, C.-L. & Li, H.-L. Electrodeposited nickel hydroxide on nickel foam with ultrahigh capacitance. *Chem. Commun.*, 6537-6539, doi:10.1039/B815647F (2008).

Acknowledgements:

This work was supported by the U.S. National Science Foundation Division of Materials Research under Award number DMR-2002634 and the Office of Naval Research (ONR) under Award No. N00014-16-1-2921. The electrochemical measurement apparatus was purchased with the help of the US Air Force Office of Scientific Research (AFOSR) Grant No. FA9550-18-1-0020. CN thanks Sheldon and Dorothea Buckler for their generous support. J.C.R. and S.R.P. are supported by the U.S. Department of Defense through the National Defense Science & Engineering Graduate Fellowship (NDSEG) Program. V.A.P. is supported by the National Science Foundation Graduate Research Fellowship Program (NSF GRFP #2019279091). D.A.R. thanks the Columbia Nano Initiative for postdoctoral fellowship support. L.E.M. thanks Columbia University for lab startup funding.

Author contributions:

J.C.R., Y.Y., X.R., C.N., and S.R.P. designed the experiments. S.R.P. and J.G. synthesized and spectroscopically characterized the materials. J.C.R. and V.A.P. fabricated devices and performed electrochemical measurements. R.M. and L.E.M. performed solid-state NMR. D.A.R. and S.R.P. performed gas adsorption analysis. H.Z. provided the activated carbon electrodes. S.R.P. and M.L.S. performed DFT modeling. All authors discussed the data and contributed to writing the manuscript.

Competing interests:

The authors declare no competing interests.

Additional information:

Supplementary Information is available for this paper.

Correspondence and requests for materials should be addressed to C.N. or X.R.

Reprints and permissions information is available at www.nature.com/reprints

Extended data:

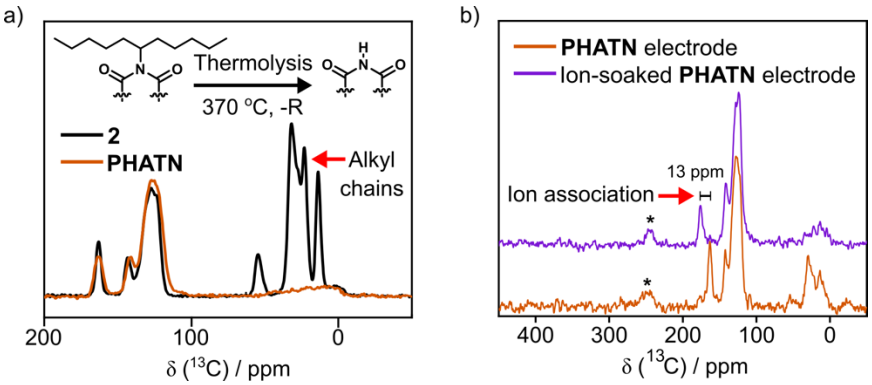

Extended Data Fig. 1. Solid state ^{13}C NMR of PHATN. (a) **Cyclized PHATN** (**2**) and the thermolyzed product (**PHATN**). Note the retention of the characteristic aromatic material peaks between δ 200-100 ppm and the disappearance of the alkyl peaks between δ 75-0 ppm, indicating the near-quantitative removal of the alkyl chains during thermolysis. (b) Solid-state ^{13}C NMR of the **PHATN** material incorporated into an electrode (see Methods for details), both as-fabricated (orange trace) and soaked in electrolyte (purple trace), showing a shift assigned to ion association to a carbonyl within the material. Asterisks denote spinning sidebands at magic angle spinning frequency of 18 kHz.

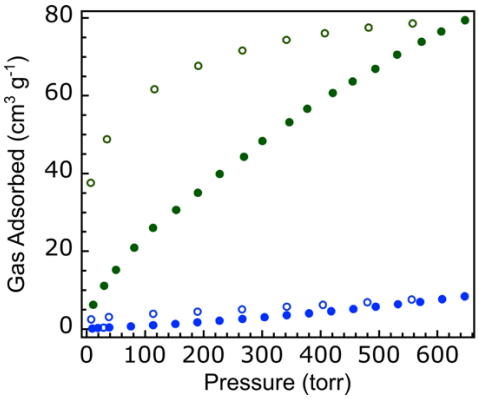

Extended Data Fig. 2. Gas adsorption measurements of PHATN and PA-PDI. Adsorption (filled symbols) and desorption (open symbols) isotherms of CO_2 for **PHATN** (dark green) and **PA-PDI** (blue) collected at -78 °C. Analysis of the **PHATN** isotherm (dark green) shows a Brunauer-Emmett-Teller surface area of 131 m^2/g, calculated using the pressure range 50–227 torr, and a Langmuir surface area of 671 m^2/g, calculated using the pressure range of 227–647 torr. However, as **PHATN** can likely undergo further structural distortions under operating conditions, these values are intended to be an estimate of the surface area and are included here for reporting purposes only. Analysis of the **PA-PDI** isotherm (blue) shows a Brunauer-

Emmett-Teller surface area of 12 m^2/g, calculated using the pressure range 50–227 torr. This is indicative of extremely low porosity, consistent with our hypothesis that contortion is crucial to the characteristic porosity shown in **PHATN**.

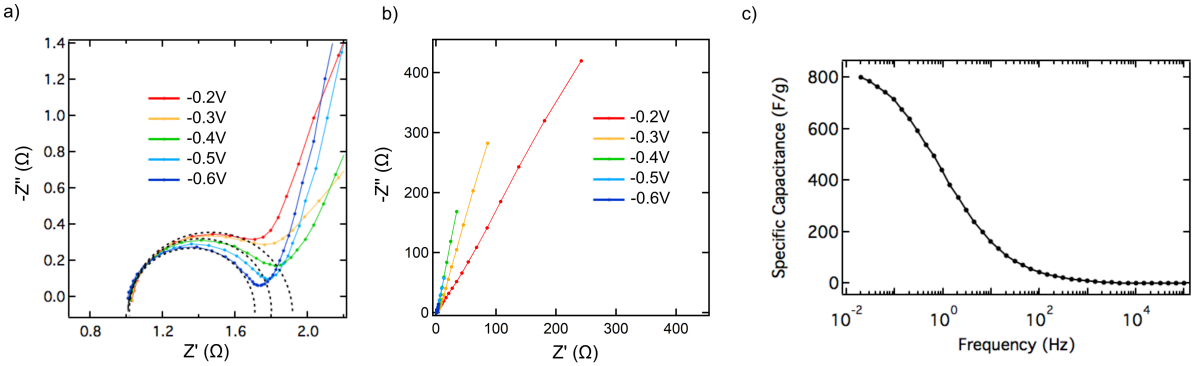

Extended Data Fig. 3. **EIS measurements performed at a range of hold potentials.** (a) High frequency region of the Nyquist plots displaying potential dependence of the diameter of the semicircular segment. The change in diameter of the semicircle with potential is indicative of a change in charge transfer resistance, as expected from a pseudocapacitive process.[50] The dotted lines are guides for the eye. (b) Low frequency region of the Nyquist plots, which shows steeper Warburg regions at more negative potentials. (c) Frequency dependence of the specific capacitance, which shows a low-frequency plateau forming near 800 F/g – near the maximum measured capacitance (689 F/g) and approaching the theoretical capacitance of the material (996 F/g). The potentials are in V vs Hg/HgO.

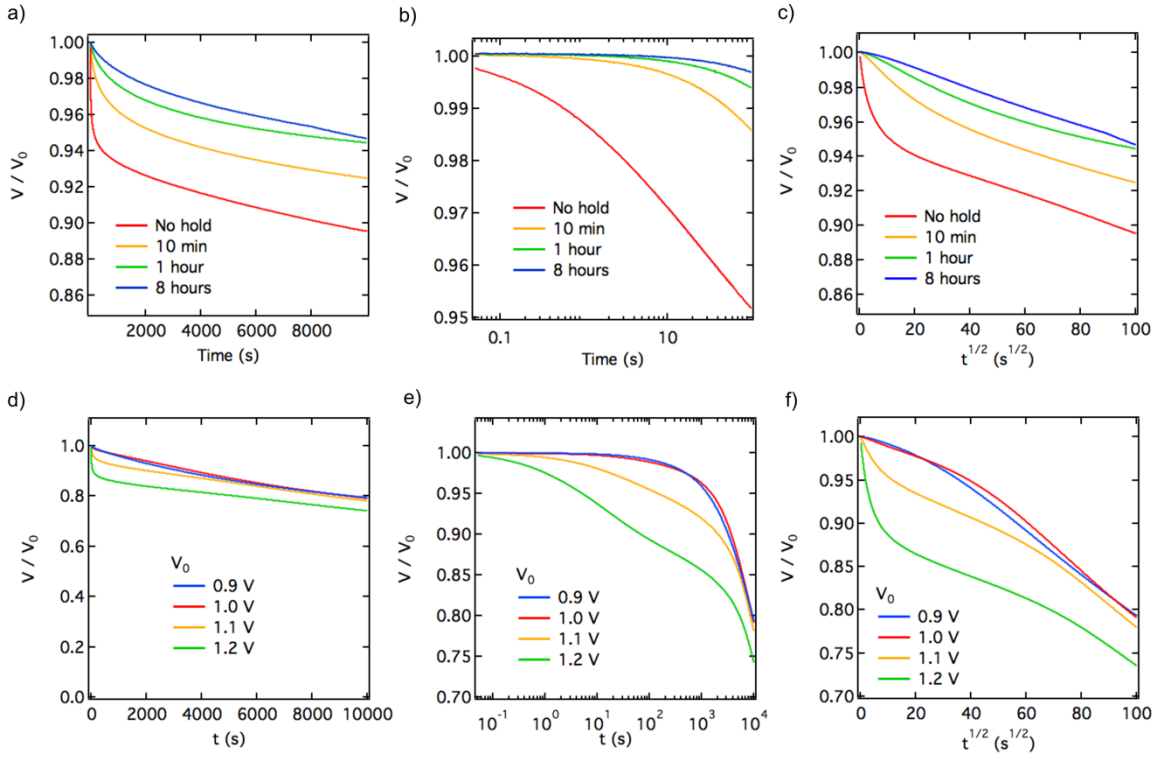

Extended Data Fig. 4. Self-discharge of PHATN in a three-electrode configuration. (a), (b), and (c) show the effect of holding the electrode at the max charge voltage before allowing to relax, with (a) in linear time, (b) in log time, and (c) in root time. (d), (e), and (f) show the effect of the max charge voltage on the self-discharge behavior, with (d) in linear time, (e) in log time, and (f) in root time.

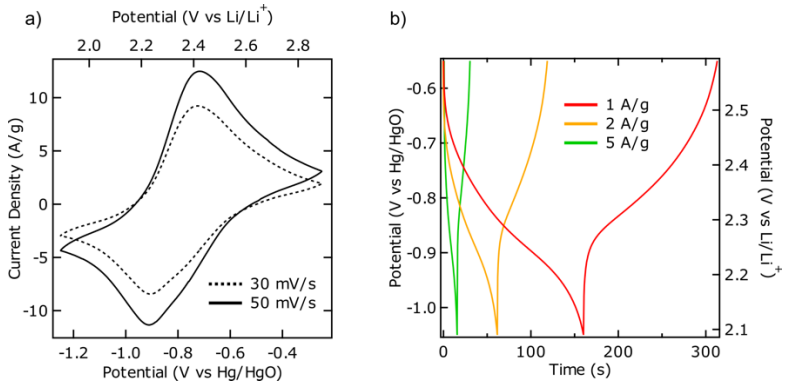

Extended Data Fig. 5. Electrochemical characterization of PA-PDI, an uncontorted control material. (a) CV of **PA-PDI** shows similar reversible redox peaks to **PHATN**, though sharper and less broad. (b) GCD of **PA-PDI** shows relatively high IR drop and less ideal triangular capacitor shape. All measurements were performed in 6 M KOH aqueous electrolyte.

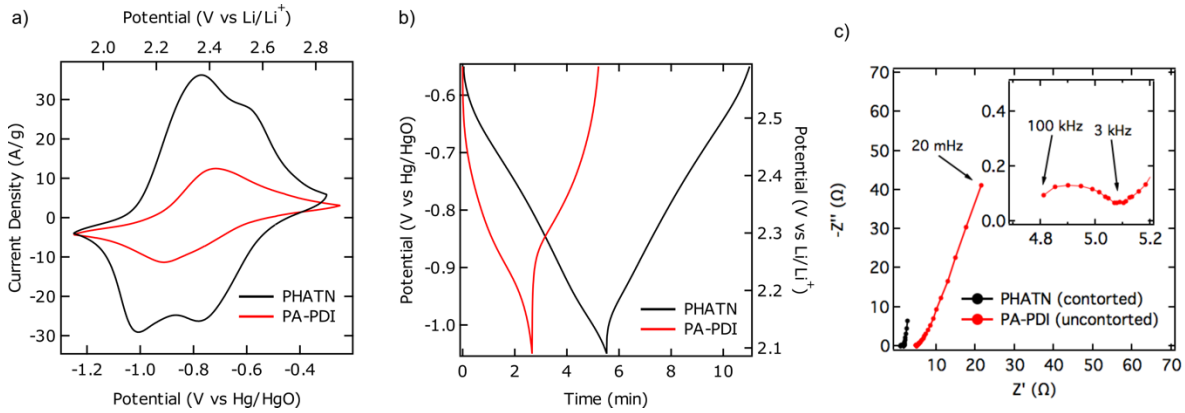

Extended Data Fig. 6. Direct electrochemical comparison of PA-PDI with PHATN. (a) CV at 50 mV/s and (b) GCD at 1 A/g. (c) Nyquist plot of **PA-PDI**, when compared to **PHATN**, displays a less steep Warburg slope in the low-frequency region, indicating less capacitive character. Both measurements are performed at -0.7 V vs Hg/HgO. Frequency range is from 100 kHz to 20 mHz.

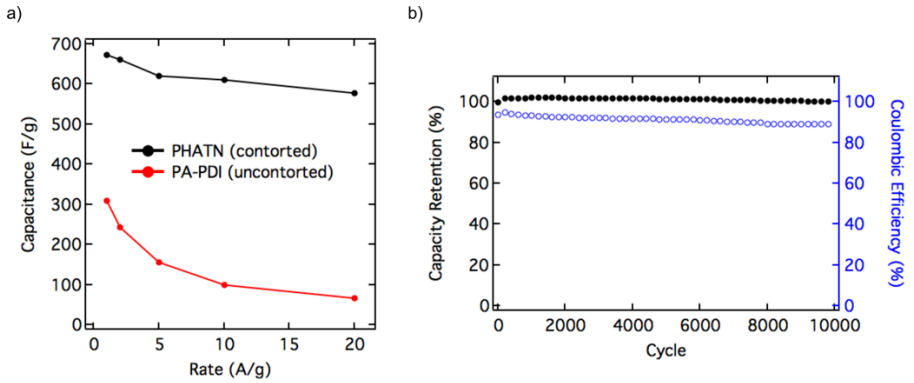

Extended Data Fig. 7. Rate and cycling performance of PA-PDI. (a) Specific capacitance values vs. rate for **PHATN** and **PA-PDI**. The latter has consistently lower performance, especially at high rates, attributable to the absence of contortion and resulting internal space which enable ion movement. (b) Capacity retention and coulombic efficiency vs. number of cycles for **PA-PDI**. The material maintains the same high stability over 10,000 cycles as **PHATN**, indicating that the polymeric material is well-formed and not affected by repeated charging and discharging.

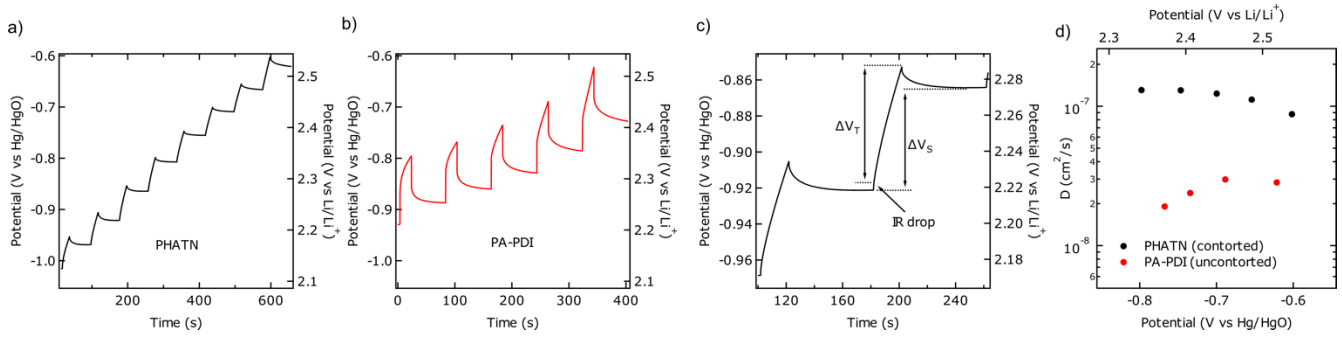

Extended Data Fig. 8. Galvanostatic intermittent titration technique (GITT) for PHATN and PA-PDI. GITT discharge curves as function of time for (a) **PHATN** and (b) **PA-PDI**. The measurements were performed at 2 A/g with 20 s current pulse and 1 min open circuit relaxation. (c) Schematic interpretation of the GITT data to estimate the diffusion constant (see below equation). (d) Diffusion coefficient (*D*) of the charge carrying species measured from GITT for **PHATN** and **PA-PDI**. Comparing the diffusion coefficients across the potential range, we observe that the diffusion coefficient of **PHATN** (~1x10^{-7} cm^2/s) is nearly one order of magnitude larger than that of **PA-PDI** (~3x10^{-8} cm^2/s), indicating that the charge carrying species (K^+) diffuses through the internal space created by contortion much more quickly, leading to the superior performance of **PHATN**. These values of ionic diffusion coefficients are comparable to reported values measured with aqueous electrolyte in porous polymeric materials.[51,52]

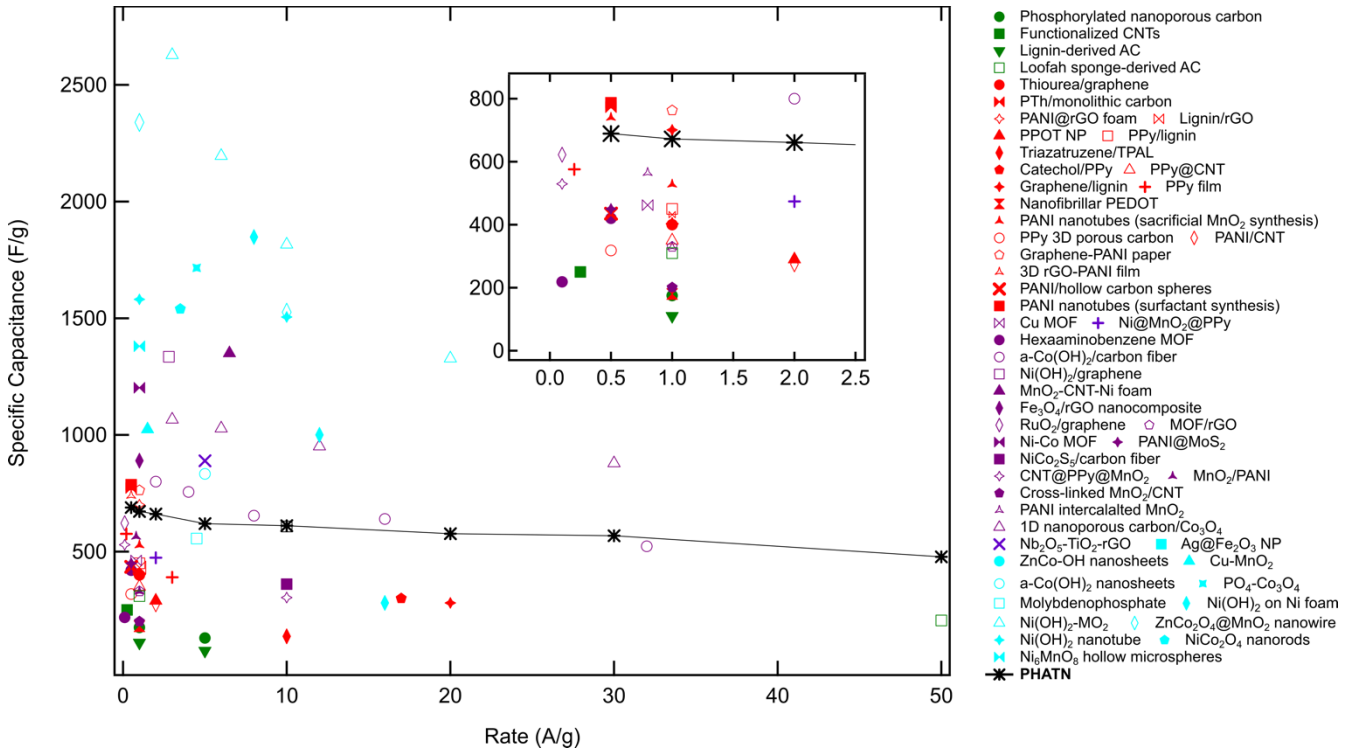

Extended Data Fig. 9. Specific capacitance as a function of current density for PHATN and a suite of benchmark materials. Green symbols are carbon-based materials;[53-56] red symbols are conducting polymer-based materials;[57-75] purple symbols are hybrid organic/inorganic materials;[76-93] and blue symbols are inorganic materials.[47,94-104] **PHATN** outperforms nearly all other pure organic materials at lower rates, and at higher rates achieves performance unprecedented in any material class besides inorganic compounds. **PHATN** values and all reference values are taken from three-electrode measurements.

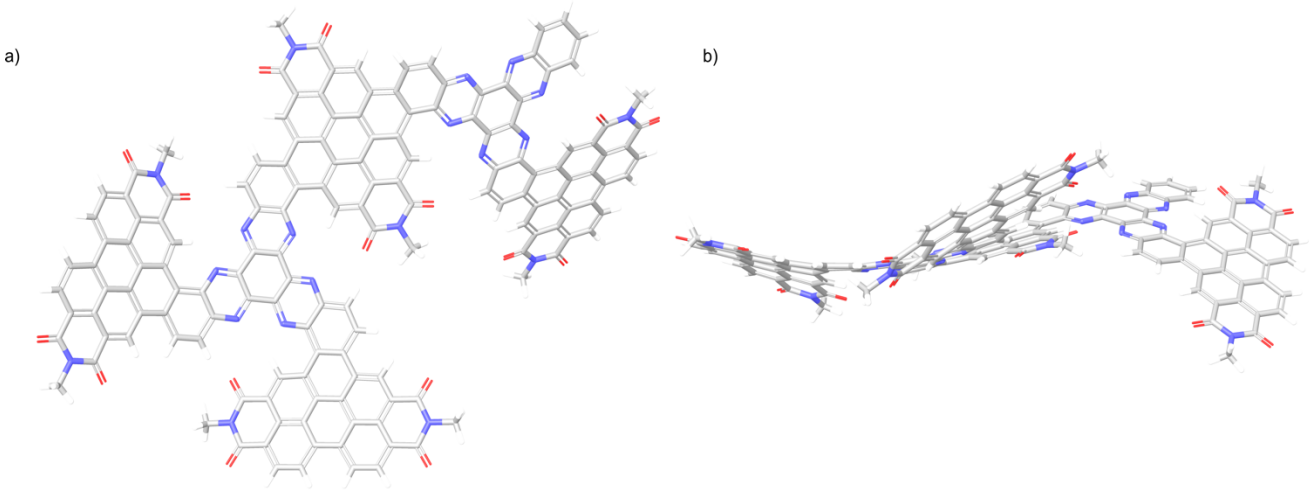

Extended Data Fig. 10. DFT model of extended PHATN. (a) Top-view and (b) side-view of the DFT energy-minimized structure of **Extended PHATN** composed of multiple units of PDI and HATN. The accessible space provided by molecular contortion is clearly visible.